Film thickness build-up in zero entrainment velocity wide point contacts

Bilel Meziane, Philippe Vergne, Nicolas Devaux, Lionel Lafarge, Guillermo Morales-Espejel, Nicolas Fillot

FILM THICKNESS BUILD-UP IN ZERO ENTRAINMENT VELOCITY WIDE POINT CONTACTS

Authors: Bilel Meziane[a]*, Philippe Vergne[a], Nicolas Devaux[a], Lionel Lafarge[a], Guillermo E. Morales-Espejel[b], Nicolas Fillot[a]

[a] Univ Lyon, INSA-Lyon, CNRS UMR5259, LaMCoS, F-69621, France

[b] SKF Research and Technology Development, 3430 DT Nieuwegein, The Netherlands

Corresponding author, nicolas.fillot@insa-lyon.fr

Abstract

In this work, elastohydrodynamic wide point contacts are studied under Zero Entrainment Velocity (ZEV) conditions. Contrary to classical rolling-sliding contacts, no hydrodynamic lift (oil wedge effect) is expected in stationary isothermal ZEV contacts. However, both experiments and numerical simulations taking into account temperature gradients in the thickness of the lubricant show the occurrence of a full-film lubrication regime over a large range of surface velocities, contact loads and external temperatures. Numerical simulations, including thermal effects but neither transient nor wall slip effects, are in good agreement with experimental film thickness measurements. They allow for both a qualitative description of the mechanisms at stake and to a first tentative minimum film thickness prediction under those specific conditions.

Keywords

Elastohydrodynamic, Film thickness, Thermal, Simulation, Zero entrainment velocity, Viscosity wedge

1 Introduction

Mechanical components such as full complement bearings present a specific kinematic configuration that leads to elastohydrodynamically lubricated (EHL) contacts between consecutive rollers where both contacting surfaces move in opposite motion[1]. EHL contacts have been studied extensively, and predictive formulae exist to determine the values of central and minimum film thicknesses in pure rolling conditions([2]–[9]). However, these formulae all assume a non-zero value of the entrainment velocity. In the case of roller to roller contacts, zero entrainment velocity (ZEV) applies and the classical predictions from the literature can no longer be used. Nevertheless, both experimental measurements and numerical simulations prove the existence of a full-film separation of the surfaces in ZEV conditions[10]. Multiple theories have been proposed to explain film

generation at ZEV, such as transient effects[11][12] or wall slip[13]. Other authors have shown that in the absence of transient effects or wall slip, a phenomenon called the viscosity wedge is the sole responsible for the existence of this film(see Yagi et al.[14][15], Bruyere et al.[16], Guo et al.[17][18][19], Yang et al.[20] and Zhang et al.[10][21][22]).

The term “viscosity wedge” was introduced by Cameron[23]. It refers to the influence of the temperature and viscosity gradients in the thickness of EHL contacts on the pressure generation[24]. In rolling/sliding contacts, Cheng[25] used the Generalized Reynolds equation[26] to take into account the variation of viscosity across the film thickness. Chiu[27] made calculations for high sliding ratios. He noted a particular “dimpled” film shape, where two local minimum film thicknesses were found on both sides along the central axis of the contact. This dimple is a feature commonly found in ZEV contacts ([10][14]–[22]).

Having two different materials for the contacting bodies is a way for heat to be evacuated differently, which means that differences in temperature between the two solids can be achieved more easily. Cameron[24] even argued that having similar solid materials cannot lead to a permanent film of lubricant. Dyson and Wilson[28] conducted experiments that proved that idea wrong. They revealed that, for two similar materials under ZEV conditions, a sufficiently low roughness on both surfaces would allow a full-film lubrication regime. In the late 90’s, the National Aeronautics and Space Administration (NASA) [1][29][30][31] showed that ZEV contacts could be operated under elastohydrodynamic conditions with the same material on both solids.

The main objective of this work is to initiate a minimum film thickness prediction under ZEV conditions. Experimental data will be used as a reference for the quantitative validation of a numerical model of ZEV line or wide point contacts. This model will provide a better understanding of the mechanisms involved in stationary Thermal ZEV contacts. From a given choice of materials and geometry, a set of operating conditions (normal loads, surface velocities and external temperatures) will be studied.

2 Experiments and numerical model description

2.1 Experiments

Experiments were conducted on a barrel-on-disk apparatus (see schematic representation in Figure 1). This tribometer was previously described by Yagi[32]. The radii of the barrel ($R_{b,x} = 0.013\ m$ and $R_{b,y} = 0.330\ m$) were fixed, with an ellipticity parameter $D = 0.04$. The lubricant was supplied on both sides of the ZEV contact (2 inlets) by a feeding system composed of an external bath (where the temperature was regulated at a value T_0), a peristaltic pump with a volumetric flow of $34\ cL/min$

and two projection nozzles oriented towards the two ZEV contact inlets. The rotational speeds of the disc and the barrel were controlled by two independent servomotors. The contact was loaded by moving the barrel up against the disk.

Practical applications of contacts under ZEV conditions often involve two steel surfaces ([1][29][30][31][12]). However, optical film thickness measurements rely on one transparent surface. As a compromise, a sapphire disk was chosen here for its thermal similarity with steel ([14][19]). Both surfaces were polished to reach an average surface roughness of $S_a = 5\ nm$.

Each operating conditions is represented by three control parameters: the external temperature T_0, the contact normal load w^{2D} and the surface velocity of the solids u. Fifty cases were studied in total, as specified in Table 1.

Film thicknesses were measured via white light Differential Colorimetric Interferometry (see [33] for a detailed description). Depending on the film thickness separating the two solids, the distance travelled by the light rays varied, leading to interferometric fringes between the light reflected on the sapphire disk lower surface and the one reflected by the steel barrel.
For each of the 50 conditions in Table 1, 6 interferograms were randomly chosen to calculate average values. Error bars, which represent the standard deviation on each set of 6 values, are reported in the corresponding figures.

2.2 Numerical model

A numerical model is proposed to access local phenomena and to enable a better understanding of ZEV contacts. Two variants of the model are considered. The two dimensional (2D, on xy-plane) model aims to describe a wide point contact. The one dimensional (1D, along x-axis) model stands for a line contact representing the behaviour along the sliding direction. The properties of the chosen materials (steel and sapphire) are summarized in Table 2 (see [34]). The value of thermal conductivity for the steel in Table 2 was chosen according to the cited source [34] even though according to [35], its value would be closer to $21\ W.m^{-1}.K^{-1}$. The lubricant chosen is Shell T9, a mineral turbine oil with few additives, used in previous studies (see [36][37]).

The fluid density is characterized by a Murnaghan[38] equation of state model (eq. 1).

$$\rho(p,T) = \rho_R \frac{1}{\left(1+\frac{K'_M}{K_M}p\right)^{-\frac{1}{K'_M}}} \frac{1}{1+a_v(T_0-T_R)} \qquad \textit{eq. 1}$$

where $K_M = K_{00}e^{-\beta_K T}$.
The fluid Newtonian behaviour is characterized by an improved WLF model[39] (eq. 2) and its non-Newtonian behaviour by a Carreau-Yasuda model[40] (eq. 3).

$$\mu(p,T) = \mu_G\left(\frac{-2.303\ C_1(T-T_g)F}{C_2 + (T-T_g)F}\right) \quad \textit{eq. 2}$$

where $T_g(p) = T_{g0} + A_1\ln(1+A_2p)$ and $F(p) = (1+B_1p)^{B_2}$

$$\eta(p,T,\tau_e) = \frac{\mu(p,T)}{\left(1+\left(\frac{\tau_e}{G_{CY}}\right)^{a_{CY}}\right)^{\frac{\frac{1}{n_{CY}}-1}{a_{CY}}}} \quad \textit{eq. 3}$$

where $\tau_e = \sqrt{{\tau_{zx}}^2 + {\tau_{zy}}^2}$ with τ_{zx} and τ_{zy} the calculated shear stresses along x and y axes respectively.

The viscosity model was fitted to experimental rheological data, obtained in a range of pressure from 0 to 800 MPa, temperature from 303 to 423K, and shear stress up to 5 MPa. The maximum error between the viscosity model (eq. 2 and 3) and the experimental data is 5%. The fluid parameters are detailed in Table 3.

The numerical model can be used for wide point contacts (2D) or line contacts (1D). It was developed and described successively by Raisin[11] and Wheeler[41]. The Generalized Reynolds equation can provide the pressure in the contact, taking into account the density and viscosity variations in the thickness of the lubricant film (eq. 4, eq. 5).

$$\vec{\nabla}\left(\left(\frac{\rho}{\eta}\right)_e \vec{\nabla}p\right) = \vec{\nabla}(\overrightarrow{\rho^*}) \quad \textit{eq. 4}$$

where $\left(\frac{\rho}{\eta}\right)_e = \frac{\eta_e}{\eta'_e}\rho'_e - \rho''_e$, $\overrightarrow{\rho^*} = \begin{pmatrix} 2u\rho'_e\eta_e + \rho_e u \\ 0 \end{pmatrix}$

and $\frac{1}{\eta_e} = \int_0^h \frac{dz}{\eta}$, $\frac{1}{\eta'_e} = \int_0^h \frac{zdz}{\eta}$, $\rho_e = \int_0^h \rho dz$, $\rho'_e = \int_0^h \left(\rho \int_0^z \frac{dz'}{\eta}\right) dz$, $\rho'_e = \int_0^h \left(\rho \int_0^z \frac{z'dz'}{\eta}\right) dz$

(1D) $$h(x) = h_0 + \frac{x^2}{2R_{eq}} + \delta(x)$$

(2D) $$h(x,y) = h_0 + \frac{x^2}{2R_{b,x}} + \frac{y^2}{2R_{b,y}} + \delta(x,y)$$ *eq. 5*

The film thickness is the sum of three terms: the rigid body separation h_0 (always negative in the context of EHL because the elastic displacements are larger than the film thicknesses), the geometrical term and the equivalent body displacement δ. Details on numerical stability method and

cavitation treatment can be found in Habchi[42]. In this study, the domain (Ω_p) where Reynolds equation is solved is adapted from Habchi[42] to comply with ZEV conditions. The domain (Ω_p) is defined as follows: $x \in [-6a^{1D}; +6a^{1D}]$ for line contacts (1D) or $x \in [-6a^{2D}; +6a^{2D}] \times y \in [-3b^{2D}; +3b^{2D}]$ for wide point contacts (2D). Zero pressure is imposed at the edges of the calculation domain (Ω_p).

The total elastic displacement of both bodies, δ, is calculated assuming an equivalent body and the load balance equation is considered. The domain (Ω_e) where the elastic body displacements are calculated is $x \in [-30a^{1D}; +30a^{1D}] \times z \in [-60a^{1D}; 0]$ for line contacts (1D) or $x \in [-30a^{2D}; +30a^{2D}] \times y \in [-30b^{2D}; +30b^{2D}] \times z \in [-60a^{2D}; 0]$ for wide point contacts (2D). A fixed constraint is applied to the bottom edge of the domain $(\Omega_{e,bot})$, and the pressure calculated via the Reynolds equation is applied to a portion of the top surface $(\Omega_{e,top})$ corresponding to (Ω_p).
The energy balance of the system is computed (eq. 6) in the lubricant volume as well as in both solids (see [11][41]).

$$-\nabla(k_i \nabla T) + \rho_i C_{pi} \vec{U}_i \nabla T = Q_i \qquad \textit{eq. 6}$$

where k_i, ρ_i and Cp_i are material characteristics that depend on the subdomain (f stands for fluid, b for barrel and d for disk) in which the equation is written ($i \in \{f, b, d\}$) and $\vec{U}_i = \begin{pmatrix} u_{i,x} \\ u_{i,y} \end{pmatrix}$. Also:

$$Q_i = \begin{cases} 0 & \text{for } i = \{b, d\} \\ \eta\left(\nabla \vec{U}_f\right)^2 - \dfrac{T}{\rho}\dfrac{\partial \rho}{\partial T}\left(\vec{U}_f \vec{\nabla} p\right) & \text{for } i = f \end{cases}$$

$$\vec{U}_b = \begin{pmatrix} +u \\ 0 \end{pmatrix}$$

$$\vec{U}_d = \begin{pmatrix} -u \\ 0 \end{pmatrix} \qquad \textit{eq. 7}$$

$$\vec{U}_f = \begin{pmatrix} u_{f,x} \\ u_{f,y} \end{pmatrix} = \begin{pmatrix} \dfrac{\partial p}{\partial x}\left(\displaystyle\int_0^z \frac{z' dz'}{\eta} - \frac{\eta_e}{\eta'_e}\int_0^z \frac{dz'}{\eta}\right) + 2u\eta_e \displaystyle\int_0^z \frac{dz'}{\eta} - u \\ \dfrac{\partial p}{\partial y}\left(\displaystyle\int_0^z \frac{z' dz'}{\eta} - \frac{\eta_e}{\eta'_e}\int_0^z \frac{dz'}{\eta}\right) \end{pmatrix}$$

To compute the energy equation, another geometry is required, in which the fluid and both solids have a geometry. The size of the fluid subdomain is $12a^{1D} \times h$ for line contacts (1D) or $6a^{2D} \times 6b^{2D} \times h$ for wide point contacts (2D). The size of the two solid subdomains is $12a^{1D} \times 3a^{1D}$ for line contacts (1D) and $6a^{2D} \times 6b^{2D} \times 3a^{2D}$ for wide point contacts (2D). The external temperature T_0 is imposed to the top and bottom external surfaces of the solids. T_0 is also imposed for the side surfaces of the solids and fluid where the local velocity $\vec{U}_i$ is oriented towards the contact area. The

other external surfaces are submitted to a nil flux boundary condition. At both solid/fluid interfaces, flux conservation is imposed.

3 Experimental and numerical results for a reference case

A 2D reference case is defined for a steel on sapphire contact, with a surface velocity $u = 5\ m/s$, an applied normal load $w^{2D} = 50\ N$ and an external temperature $T_0 = 293.15\ K$. It represents a central situation among the variety of cases presented in Table 1. Experimental and numerical results will be compared and the model assumptions discussed. Then the viscosity wedge process will be discussed to explain the asymmetries observed in both experiments and simulations.

3.1 Description of the experimental film thickness profiles

Figure 2 is an interferogram captured according to the technique previously described. The film thickness variation along the vertical dashed central line is reported in Figure 3. At both lateral sides of the contact, two lobes can be seen and are marked by the letter “A”. Those side lobes were first described by Guo[19] and are the location of the global minimum film thicknesses. They are limited to the lateral sides and do not extend to the edge of the exit zone, unlike what is observed in conventional EHD contacts.

The central film thickness h_c is marked by the letter “B” in Figure 3. A typical feature of ZEV contacts is the fact that this central film thickness is a local maximum located at the center of a dimple.

Two local minimum film thicknesses can also be found along the vertical dashed line, located close to the inlet/outlet areas of the contact. They are noted by the letters “C” and “D” in Figure 3. Their values differ slightly from one another ([19][15][10][43]) because of the dissimilarity in the properties of the solid materials in contact (see section 3.3). The highest local minimum film thickness is called h_m^+ and the lowest one is called h_m^-. The average value of the two will be referred to as the minimum film thickness and will be noted h_m.

3.2 Discussion on model assumptions

For rolling EHD contacts, Nijenbanning[44] found that the film thickness along the central line of a wide point contact (2D) with $D < 0.1$ could be described by a line contact (1D) model. In this case, the barrel-on-plane contact is considered similar to a cylinder-on-plane contact. An equivalent line contact (1D) is defined by keeping the same Hertz pressure ($p_h^{1D} = p_h^{2D}$) and same contact length ($a^{1D} = a^{2D}$) by choosing R_{eq} and w^{1D} as in eq. 8:

$$\begin{cases} p_h^{1D} = p_h^{2D} \\ a^{1D} = a^{2D} \end{cases} \Leftrightarrow \begin{cases} R_{eq} = E' a^{2D}/4p_h^{2D} \\ w^{1D} = \pi p_h^{2D} a^{2D}/2 \end{cases} \qquad \textit{eq. 8}$$

The corresponding reference case in 1D is written with a corresponding normal load per unit length $w^{1D} = 5.82 \times 10^4\ N.m^{-1}$.

The experimental film thickness profile along the vertical central line is represented in Figure 3. On the same figure, point contact (2D) and line contact (1D) numerical results are superimposed.

The numerical (2D) central film thickness is very close to the experimental value (deviation of 2.8%). The numerical (2D) minimum film thickness overestimates the measurements by 23.9%, which is comparable to deviations between simulations and analytical predictions reported in [36] for classical pure rolling conditions.

The (1D) numerical central film thickness is 28.3% lower than the experimental one and the (1D) numerical minimum film thickness is 3.3% larger than the experimental one, with h_m^+ and h_m^- being 0.2% and 6.9% larger respectively which is exceptionally good with respect to the differences observed with the (2D) model. With this in mind, and with the close results between (1D) and (2D) models, the (1D) model will be retained in the rest of this document.

3.3 Viscosity wedge and material dissimilarity

In section 2.1, the fact that the thermal conductivity of steel may differ was noted. A (1D) simulation was conducted, with the same parameters as the (1D) reference case, but with a thermal conductivity of $21\ W.m^{-1}.K^{-1}$[35]. It is plotted in Figure 4. There is less than a 4% relative difference between the values of minimum and central film thicknesses found for the two cases, which indicates that the parameters in Table 2 are representative of the chosen steel in any case.

The differences between h_m^+ and h_m^- seen in 3.1 and Figure 3 can be explained by the fact that the solids in contact are made of materials that differ in thermo-mechanical properties (see [43]). Figure 5 shows the temperature distribution in the reference case with h_m^+ on the right and h_m^- on the left. The fluid external temperature conditions being the same on both sides far away from the contact area, the temperature of the fluid at the two inlets in the proximity of the surfaces entering the contact, is the same as indicated by the mention "T_0" in Figure 4. The viscosity wedge process develops as follows: the top surface goes from the left to the right and the bottom one from the right to the left. This creates a very intense shearing and the fluid heats up before exiting on the right side for the top surface and left side for the bottom one. This leads to high temperature gradients across the film thickness on both sides near the edges of the contact. The values of temperature and viscosity differences along the x-axis are plotted in Figure 4.

The Navier-Stokes equation applied to thin films can be used to link pressure generation with the viscosity differences. For the line contact:

$$\frac{\partial p}{\partial x} = \frac{\partial(\eta\dot{\gamma})}{\partial z} \qquad \textit{eq. 9}$$

This equation is the basis for Generalized Reynolds equation, which assumes that the pressure does not vary along $\vec{z}$. By making the same assumption for eq. 9, an average value of this equation can be calculated between $z = 0$ and $z = h$:

$$\frac{\partial p}{\partial x} = \frac{1}{h}\int_0^h \frac{\partial p}{\partial x} dz = \frac{1}{h}\int_0^h \frac{\partial(\eta\dot{\gamma})}{\partial z} dz = \frac{(\eta\dot{\gamma})_h - (\eta\dot{\gamma})_0}{h} = \frac{\Delta(\eta\dot{\gamma})}{h} \qquad \textit{eq. 10}$$

Pressure generation is proportional to the viscosity times shear rate difference between the two surfaces. This mechanism explains the load bearing capacity due to temperature gradients across the film thickness.

This mechanism also explains the rather low asymmetry observed in sapphire/steel contacts. Because the thermal characteristics of both solids differ, heat is not exchanged at the same rate at each both fluid/solid interface. Indeed, for the reference case, a power per unit length of $7285\ W/m$ is being evacuated through the fluid/steel interface while $7055\ W/m$ is transferred through the fluid/sapphire interface. This leads to different maximum surface temperatures for both interfaces: $316\ K$ for the former and $321\ K$ for the latter.
In Figure 4, the temperature differences between the surfaces is larger on the left side of the contact. The maximum viscosity differences found in the vicinity of the two surfaces, which occur mainly in the zone where the pressure is high (due to the pressure dependence of the viscosity), are of $48.2\ Pa.s$ and $7.0\ Pa.s$ on the left and right sides respectively. With more pressure generated on the left side of the contact, the pressure and displacement profiles are slightly shifted to the right. This explains the asymmetry observed in the film thickness. In Figure 4, the equivalent steel-on-steel calculation gives a symmetrical film thickness profile. For the reference case, the relative difference between h_m^+ and h_m^- is 4.0% experimentally and 11.3% numerically. The average value between h_m^+ and h_m^-, called h_m, will be used primarily in the rest of this document to describe the minimum film thickness.

Knowledge on the minimum film thickness and its prediction are of particular interest, since it has to be compared to surface roughness to anticipate the possible occurrence of solid to solid contacts. In the next section, the influence of the surface velocity on the minimum and central film thicknesses are studied for ZEV wide contacts by using the (1D) model, upon various load and external temperature conditions.

4 Film thickness dependence on surface velocity, at various loads and external temperatures

In this section, the experimental results are compared with the line contact (1D) model for various surface velocities, loads and external temperatures.

4.1 Influence of the surface velocity

The surface velocity u is varied, for a normal load per unit length $w^{1D} = 5.82 \times 10^4\ N.m^{-1}$ and an external temperature $T_0 = 293.15$ K. The numerical model enables the calculation of film thicknesses at higher velocities (up to $u = 17.7\ m/s$) than the limitation imposed by the test-rig ($u = 7.92\ m/s$). The variations of experimental and numerical (line contact), central and minimum film thicknesses are represented in Figure 6. In these conditions, the line contact (1D) model enables the accurate prediction of the minimum film thickness for any surface velocity, with the relative difference between experimental and numerical results between 0.3% and 11.6%. There is a steady increase of both experimental and numerical minimum film thicknesses with the surface velocity up to $u = 10\ m/s$. This corresponds to the variations observed in the literature ([17][15][16][10]).

The higher the surface velocity, the stronger the convection term in the energy equation. This directly impacts the location of the maximum temperature difference along the surfaces, as seen in Figure 7. Indeed, at $1.77\ m/s$ the location of the maximum temperature difference between the two surfaces is $34\ \mu m$ to the left of the contact center whereas it is $65\ \mu m$ away at $7.92\ m/s$. Therefore, both the maximum viscosity differences and pressure gradients are found further away from the contact center. In Figure 7 at $1.77\ m/s$, the maximum pressure gradient is 2.1×10^{13} Pa/m and located $34\ \mu m$ to the left of the contact center whereas at $7.92\ m/s$, the maximum pressure gradient is 9.0×10^{12} Pa/m and located $62\ \mu m$ away from the center of the contact. In conclusion, the convection term increases with the surface velocity and shifts the location of maximum pressure gradients away from the center which corresponds to higher minimum film thicknesses.

In Figure 6, though shifted by nearly $130\ nm$ (relative difference between 14.2% and 28.1%), the experimental and numerical results show nearly no variation of the central film thickness with the surface velocity, as mentioned in ([17][15][16][10]). Pressure is generated closer to the center for smaller velocities. To comply with the load balance equation, this leads to bigger central pressures. Indeed, at $1.77\ m/s$, the central pressure is $0.79\ GPa$ when it is only $0.48\ GPa$ at $7.92\ m/s$, a 64% difference (see Figure 8). This leads to a central displacement at $1.77\ m/s$ which is 8% larger than at $7.92\ m/s$. All the while, the rigid body separation is larger by a similar margin of 11%. To summarize, as the surface velocity increases, the rigid body separation increases while the central displacement decreases at a similar rate due to the wider pressure generation, which explains why the central film thickness barely varies with the surface velocity.

In Figure 6, at high velocities not accessible with the experiments, the numerical central and minimum film thicknesses 1D predictions become the same, indicating the disappearance of the central dimple. The film thickness decrease at the highest velocities is linked to a wider pressure profile, as can be seen in Figure 8. At the centre, the pressure decreases (leading to less surface displacement), which corresponds to a central/minimum film thickness decrease.

A mean square power law approximation of the minimum film thickness variation with the surface velocity is plotted in Figure 6, for $u \in [1.77; 7.92] m/s$. In this case, the minimum film thickness varies with the surface velocity to a power 0.51, which is less than the one found for the entrainment velocity in rolling contacts([8][9]). Additionally, a power law approximation is not able to describe the complete behaviour over the full range of velocities.
A more complex formula is written to fit the plateau-like behaviour observed at high velocities:

$$h_m = h_{lim} \times (1 - \exp(-u/u_{lim})) \qquad \textit{eq. 10}$$

where $h_{lim} = 345\ nm$ and $u_{lim} = 2.8\ m/s$, which respectively represent the film thickness plateau at high velocities and the inverse of the exponential decay constant. Their values are functions of all other parameters in the problem, which is the limit imposed by such a simplistic description.

4.2 Extension to various load cases

The variations of experimental and numerical (line model), central and minimum film thicknesses with the surface velocity u is represented for different normal loads in Figure 9. For the central film thickness, the relative difference between experiments and numerical results is between 14.2% and 34.8%. For the minimum film thickness, the relative difference between experiments and numerical results is between 0.3% and 15.5%. The qualitative behaviour is well captured for both the central and minimum film thickness, although only the latter is well predicted quantitatively. Experimentally, for the lower load, the increase of the central film thickness is monotonous, whereas for the higher load, a sharp increase at low velocities is followed by a rather constant decrease at higher velocities. A similar observation is made numerically, although no sharp increase is observed at higher loads and lower velocities. Both the central and minimum film thicknesses increase as the normal load increases for any surface velocity, which is a counter-intuitive result compared to the behaviour of classical rolling/sliding EHD contacts. This trend has also been confirmed for a range of loads in previous works, for line contacts [16] and for point contacts [10]. The present results bring experimental confirmation for line contacts. At $1.77\ m/s$, the minimum film thickness at $100\ N$ is 5.8% larger than at $30\ N$ whereas at $7.92\ m/s$, the increase is 8.9%. This means that the applied load has a relatively weak effect on the measured minimum film thickness for any velocity compared to other parameters as shown in ([17][15][16][10]).

Film thickness results from the sum of three terms which are affected by a change in contact normal load, as seen in eq. 5. First, as the load increases at $u = 5\ m/s^{-1}$ and $T_0 = 293.15$ K, a diminution of the rigid body separation h_0 is observed from -0.86 µm at $30\ N$ to -2.07 µm at $100\ N$. Second, the contact widens with an increasing load: the distance between the locations of h_m^+ and h_m^- is 0.10 µm at $30\ N$ and 0.17 µm at $100\ N$.Therefore, the location of the minimum film thickness is deported outwards, which means that the geometrical term of the film thickness ($x^2/2R_{eq}$) is increased from 0.11 µm at $30\ N$ to 0.27 µm at $100\ N$. Third, increasing the load generates stronger displacements in the whole contact. Indeed, at the location of the minimum film thickness, the displacement δ is increased from 1.03 µm at $30\ N$ to 2.11 µm at $100\ N$. In the end, these variations compensate each other and this explains the weak variations of the minimum film thickness with the normal load, and even in some cases the increase of the film thickness with normal load.

4.3 Extension to various temperature cases

Figure 10 shows the central and minimum film thickness variations with the surface velocity for three different external temperatures ($T_0 \in \{293.15; 308.15; 323.15\} K$). Few experimental data points were obtained at $T_0 = 308.15\ K$ and $T_0 = 323.15\ K$ due to the minimum film thickness occurring on the sides (identified as zone A in Figure 2) becoming too low to safely continue measurements at lower velocities. The values of central film thickness obtained numerically underestimate the experimental values. For the minimum film thickness, the highest relative difference between the experiments and the simulations is of 11.6%, 22.2% and 23.5% at respectively 293.15 K, 308.15 K and 323.15 K. An increase in external temperature leads to a decrease of both the central and minimum film thicknesses.

The viscosity at ambient pressure is overall higher at 293.15 K ($0.020\ Pa.s$) than at 323.15 K ($0.006\ Pa.s$). Therefore, the viscosity variations across the lubricant thickness are by far larger at lower temperatures, as can be seen in Figure 11. The maximum value of $\Delta\eta$ is $48.2\ Pa.s$ at 293.15 K and $4.2\ Pa.s$ at 323.15 K. Moreover, this maximum is found further away from the contact center at lower temperatures (8.62 µm to the left of the contact center at 293.15 K and 4.32 µm at 323.15 K) which is linked to a larger pressure generation, as can also be seen in Figure 11. This also leads to a lower central pressure at lower temperatures, as seen in Figure 12, given the load balance must been satisfied. Indeed, the central pressure is $5.62 \times 10^8\ Pa$ at 293.15 K and $7.05 \times 10^8\ Pa$ at 323.15 K, a 25% increase. As a consequence, the central displacement is larger for hotter contacts but not enough to compensate for the decreasing rigid body separation. This explains why the central film thickness decreases with the temperature.

5 Conclusion

Experiments were conducted on wide point contacts in Zero Entrainment Velocity conditions. A numerical model of thermal elastohydrodynamic contacts was also developed and used to provide useful information on local quantities such as the pressure, the temperature or the viscosity profiles. The experimental results demonstrated that significant film thicknesses exists in ZEV conditions for wide point contacts. Because neither transient effects nor wall slip were implemented in the model, the generation of a film thickness has been attributed to the viscosity wedge effect only.

The comparison of the results obtained by the two approaches has revealed that line contact models can be used to quantitatively represent the variations of the minimum film thicknesses of a wide point ZEV contact. In the worst case (high external temperature), the minimum film thickness was predicted with an accuracy of 23.5%.

Over the range of the tested parameters, the minimum film thickness increases with the surface velocity while the central film thickness has shown a non-monotonous response. At high velocities, the central dimple disappears as the central and minimum film thicknesses become equal. Over the range of tested velocities, an exponential fit describes the variation of minimum film thickness better than a power law.

The higher the load, the higher the central film thickness because the load is mainly supported at the centre. The effect on minimum film thickness is less visible.

The increase of the external temperature leads to a decrease of both the minimum and central film thicknesses. At high external temperatures, the viscosity gradients are less pronounced.

The set of results presented in this work obtained from both experimental and numerical studies enables the understanding of the film thickness build-up mechanism in ZEV conditions and constitutes a first basis on which semi-analytical tools could be written.

6 Acknowledgements

This work was funded by the Lubricated Interfaces for the Future research chair established between INSA Lyon and the SKF Company.

7 References

[1] W. R. J. Jones, B. A. Shogrin, and E. P. Kingsbury, “Long term performance of a retainerless bearing cartridge with an oozing flow lubricator for spacecraft applications,” *NASA TM-107492*. 1997.

[2] A. M. Ertel, “In Russian (Hydrodynamic Lubrication Based on New Principles),” *Nauk SSSR Prikadnaya Math. i Mekhanika*, vol. 3, no. 2, pp. 41–52, 1939.

[3] A. N. Grubin and I. E. Vinogradova, “In Russian (Investigation of the contact of machine components),” *Cent. Sci. Res. Inst. Technol. Mech. Eng.*, vol. 30, 1949.

[4] B. J. Hamrock and D. Dowson, “Isothermal Elastohydrodynamic Lubrication of Point Contacts -

I - Theorectical Formulation," *J. Lubr. Tech*, vol. 98, no. 2, pp. 223–228, 1976.
[5] B. J. Hamrock and D. Dowson, "Isothermal Elastohydrodynamic Lubrication of Point Contacts - III - Fully Flooded Results," *J. Lubr. Tech*, vol. 99, no. 2, pp. 264–275, 1977.
[6] B. J. Hamrock and D. Dowson, "Isothermal Elastohydrodynamic Lubrication of Point Contacts - IV - Starvation Results," *J. Lubr. Tech*, vol. 99, no. 1, pp. 15–23, 1977.
[7] H. Moes, "Optimum similarity analysis with applications to elastohydrodynamic lubrication," *Wear*, vol. 159, no. 1, pp. 57–66, 1992.
[8] R. J. Chittenden, D. Dowson, J. F. Dunn, and C. M. Taylor, "A Theoretical Analysis of the Isothermal Elastohydrodynamic Lubrication of Concentrated Contacts. I. Direction of Lubricant Entrainment Coincident with the Major Axis of the Hertzian Contact Ellipse," *Proc. R. Soc. A Math. Phys. Eng. Sci.*, vol. 397, no. 1813, pp. 245–269, 1985.
[9] H. P. Evans, "The Isothermal Elastohydrodynamic Lubrication of Spheres," *J. Tribol.*, vol. 103, no. 4, p. 547, Oct. 1980.
[10] B. Zhang, J. Wang, M. Omasta, and M. Kaneta, "Effect of fluid rheology on the thermal EHL under ZEV in line contact," *Tribol. Int.*, vol. 87, no. February, pp. 40–49, 2015.
[11] J. Raisin, N. Fillot, D. Dureisseix, P. Vergne, and V. Lacour, "Characteristic times in transient thermal elastohydrodynamic line contacts," *Tribol. Int.*, vol. 82, no. PB, pp. 472–483, Feb. 2015.
[12] J. Raisin, N. Fillot, P. Vergne, D. Dureisseix, and V. Lacour, "Transient Thermal Elastohydrodynamic Modeling of Cam–Follower Systems: Understanding Performance," *Tribol. Trans.*, vol. 59, no. 4, pp. 720–732, Jul. 2016.
[13] P. L. Wong, X. M. Li, and F. Guo, "Evidence of lubricant slip on steel surface in EHL contact," *Tribol. Int.*, vol. 61, pp. 116–119, May 2013.
[14] K. Yagi, K. Kyogoku, and T. Nakahara, "Temperature measurements of oil film and surface in point contact EHL under high slip ratio condition," *Toraibarojisuto/Journal Japanese Soc. Tribol.*, vol. 46, no. 9, pp. 725–732, 2001.
[15] K. Yagi, K. Kyogoku, and T. Nakahara, "Relationship Between Temperature Distribution in EHL Film and Dimple Formation," *J. Tribol.*, vol. 127, no. 3, p. 658, 2005.
[16] V. Bruyere, N. Fillot, G. E. Morales-Espejel, and P. Vergne, "Computational fluid dynamics and full elasticity model for sliding line thermal elastohydro dynamic contacts," *Tribol. Int.*, vol. 46, no. 1, pp. 3–13, 2012.
[17] F. Guo, P. Yang, and P. L. Wong, "On the thermal elastohydrodynamic lubrication in opposite sliding circular contacts," *Tribol. Int.*, vol. 34, no. 7, pp. 443–452, 2001.
[18] F. Guo, P. Yang, and S. Qu, "On the Theory of Thermal Elastohydrodynamic Lubrication at High Slide-Roll Ratios—Circular Glass-Steel Contact Solution at Opposite Sliding," *J. Tribol.*, vol. 123, no. 4, p. 816, 2001.
[19] F. Guo, P. L. Wong, P. Yang, and K. Yagi, "Film Formation in EHL Point Contacts under Zero Entraining Velocity Conditions," *Tribol. Trans.*, vol. 45, no. 4, pp. 521–530, 2002.
[20] P. Yang, S. Qu, Q. Chang, and F. Guo, "On the Theory of Thermal Elastohydrodynamic Lubrication at High Slide-Roll Ratios—Line Contact Solution," *J. Tribol.*, vol. 123, no. 1, p. 36, 2001.
[21] B. Zhang and J. Wang, "Enhancement of thermal effect in zero entrainment velocity contact under low surface velocity," *Proc. Inst. Mech. Eng. Part J J. Eng. Tribol.*, vol. 230, no. 12, pp. 1554–1561, Dec. 2016.
[22] B. Zhang, J. Wang, M. Omasta, and M. Kaneta, "Variation of surface dimple in point contact thermal EHL under ZEV condition," *Tribol. Int.*, vol. 94, pp. 383–394, 2016.
[23] A. Cameron, "The Viscosity Wedge," *A S L E Trans.*, vol. 1, no. 2, pp. 248–253, Jan. 1958.
[24] A. Cameron, "Hydrodynamic Lubrication of Rotating Disks in Pure Sliding. A new Type of Oil Film Formation," *J. Inst. Pet.*, vol. 37, no. 11, pp. 471–486, 1951.
[25] H. S. Cheng, "A Refined Solution to the Thermal-Elastohydrodynamic Lubrication of Rolling and Sliding Cylinders," *A S L E Trans.*, vol. 8, no. 4, pp. 397–410, Jan. 1965.
[26] D. Dowson, "A generalized Reynolds equation for fluid-film lubrication," *Int. J. Mech. Sci.*, vol.

4, no. 2, pp. 159–170, Mar. 1962.
[27] Y. P. Chiu and L. B. Sibley, “Contact shape and non-Newtonian effects in elastohydrodynamic point contacts,” *ASLE Lubr. Eng.*, vol. 28, pp. 48–60, 1972.
[28] A. Dyson and A. R. Wilson, “Film Thicknesses in Elastohydrodynamic Lubrication at High Slide/Roll Ratios,” *Proc. Inst. Mech. Eng. Conf. Proc.*, vol. 183, no. 16, pp. 81–97, Sep. 1968.
[29] B. A. Shogrin, W. R. Jones, E. P. P. Kingsbury, M. J. Jansen, and J. M. Prahl, “Experimental Study of Load Carrying Capacity of Point Contacts at Zero Entrainment Velocity,” *NASA TM-208650*. 1998.
[30] B. A. Shogrin, W. R. Jones, E. P. Kingsbury, and J. M. Prahl, “Experimental determination of load carrying capacity of point contacts at zero entrainment velocity,” *NASA TM-208848*. 1999.
[31] P. Thompson, “The effect of sliding speed on film thickness and pressure supporting ability of a point contact under zero entrainment velocity conditions,” *NASA TM-210566*. 2000.
[32] K. Yagi, P. Vergne, and T. Nakahara, “In situ pressure measurements in dimpled elastohydrodynamic sliding contacts by Raman microspectroscopy,” *Tribol. Int.*, vol. 42, no. 5, pp. 724–730, May 2009.
[33] T. Doki-Thonon, N. Fillot, G. E. Morales Espejel, M. Querry, D. Philippon, N. Devaux, and P. Vergne, “A Dual Experimental/Numerical Approach for Film Thickness Analysis in TEHL Spinning Skewing Circular Contacts,” *Tribol. Lett.*, vol. 50, no. 1, pp. 115–126, Apr. 2013.
[34] S.-N. Ndiaye, L. Martinie, D. Philippon, N. Devaux, and P. Vergne, “A Quantitative Friction-Based Approach of the Limiting Shear Stress Pressure and Temperature Dependence,” *Tribol. Lett.*, vol. 65, no. 4, p. 149, Dec. 2017.
[35] T. Reddyhoff, A. Schmidt, and H. Spikes, “Thermal Conductivity and Flash Temperature,” *Tribol. Lett.*, vol. 67, no. 1, p. 22, Mar. 2019.
[36] J.-D. Wheeler, J. Molimard, N. Devaux, D. Philippon, N. Fillot, P. Vergne, and G. E. Morales-Espejel, “A Generalized Differential Colorimetric Interferometry Method: Extension to the Film Thickness Measurement of Any Point Contact Geometry,” *Tribol. Trans.*, vol. 61, no. 4, pp. 648–660, Jul. 2018.
[37] T. Doki-Thonon, N. Fillot, P. Vergne, and G. E. Morales Espejel, “Numerical insight into heat transfer and power losses in spinning EHD non-Newtonian point contacts,” *Proc. Inst. Mech. Eng. Part J J. Eng. Tribol.*, vol. 226, no. 1, pp. 23–35, 2012.
[38] F. D. Murnaghan, “The Compressibility of Media under Extreme Pressures,” *Proc. Natl. Acad. Sci.*, vol. 30, no. 9, pp. 244–247, Sep. 1944.
[39] S. Bair, C. Mary, N. Bouscharain, and P. Vergne, “An improved Yasutomi correlation for viscosity at high pressure,” *Proc. Inst. Mech. Eng. Part J J. Eng. Tribol.*, vol. 227, no. 9, pp. 1056–1060, Sep. 2013.
[40] S. Bair, “A Rough Shear-Thinning Correction for EHD Film Thickness,” *Tribol. Trans.*, vol. 47, no. 3, pp. 361–365, Jul. 2004.
[41] J.-D. Wheeler, N. Fillot, P. Vergne, D. Philippon, and G. Morales Espejel, “On the crucial role of ellipticity on elastohydrodynamic film thickness and friction,” *Proc. Inst. Mech. Eng. Part J J. Eng. Tribol.*, vol. 230, no. 12, pp. 1503–1515, Dec. 2016.
[42] W. Habchi, D. Eyheramendy, S. Bair, P. Vergne, and G. Morales-Espejel, “Thermal elastohydrodynamic lubrication of point contacts using a Newtonian/generalized Newtonian lubricant,” *Tribol. Lett.*, vol. 30, no. 1, pp. 41–52, 2008.
[43] J. Raisin, N. Fillot, P. Vergne, and D. Dureisseix, “Numerical simulation of lubricated DLC-coated point contacts under infinite sliding conditions,” *Tribol. Int.*, vol. 133, pp. 136–151, May 2019.
[44] G. Nijenbanning, C. H. Venner, and H. Moes, “Film thickness in elastohydrodynamically lubricated elliptic contacts,” *Wear*, vol. 176, no. 2, pp. 217–229, Aug. 1994.

Figures

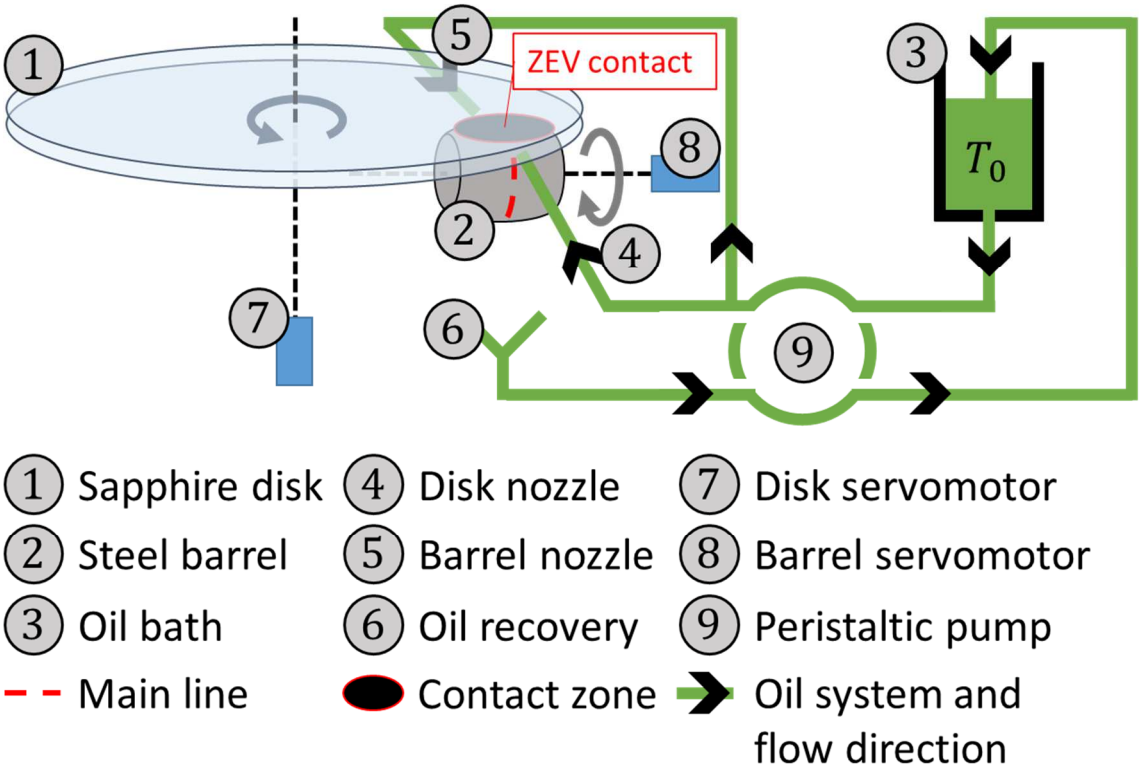

Figure 1 – Representation of the experimental apparatus.

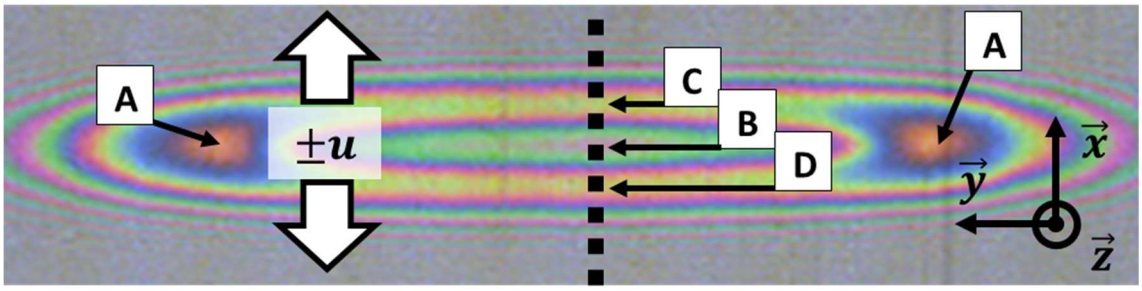

Figure 2 – White light interferogram for the reference case ($u = 5\ m/s$, $w^{2D} = 50\ N$ and $T_0 = 293.15\ K$).

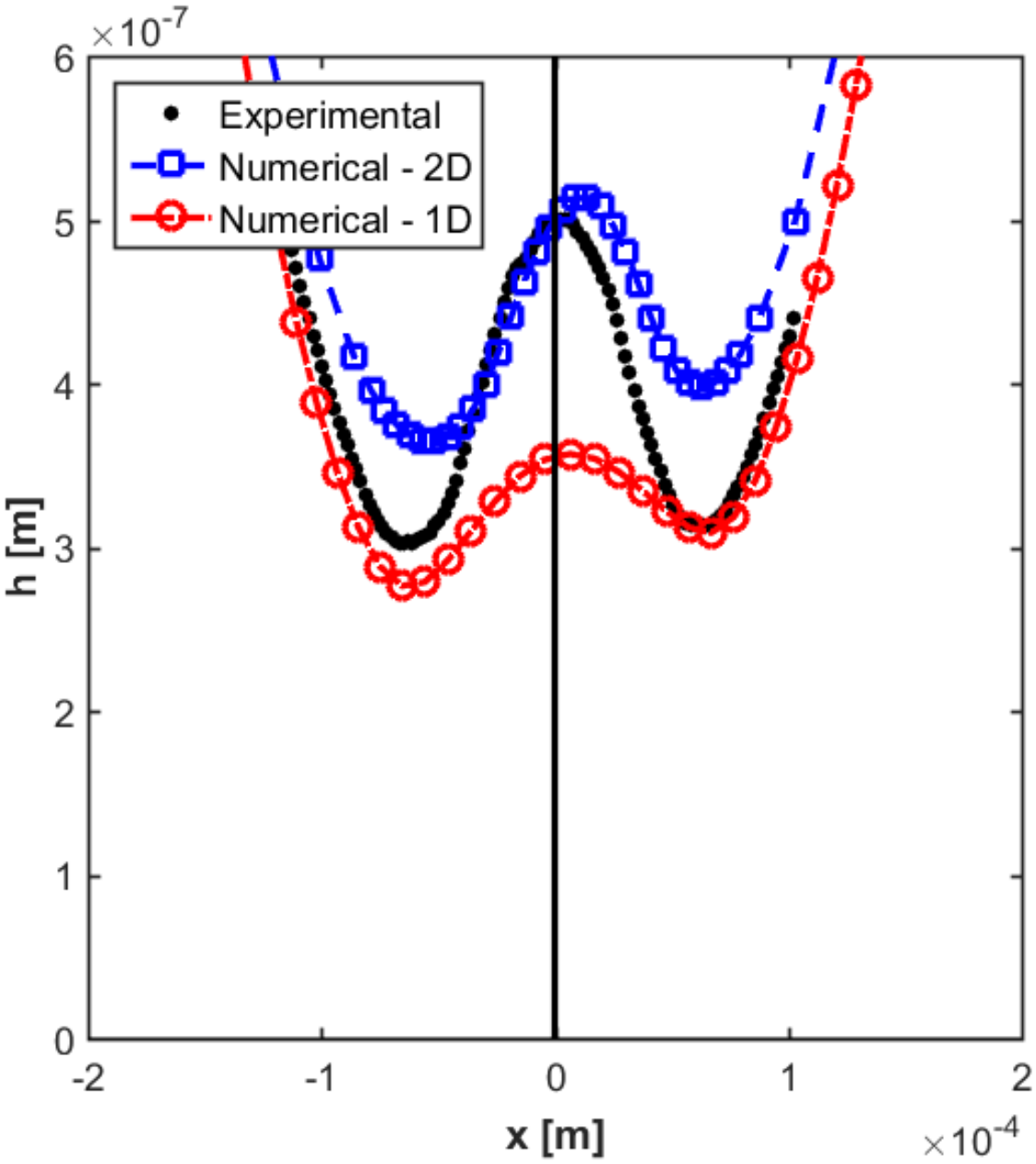

Figure 3 – Film thickness profiles for the reference case ($u = 5\ m/s$, $w^{2D} = 50\ N$ or $w^{1D} = 5.82 \times 10^4\ N.m^{-1}$ and $T_0 = 293.15\ K$), from experiments (along the dashed line in Figure 2) and simulations.

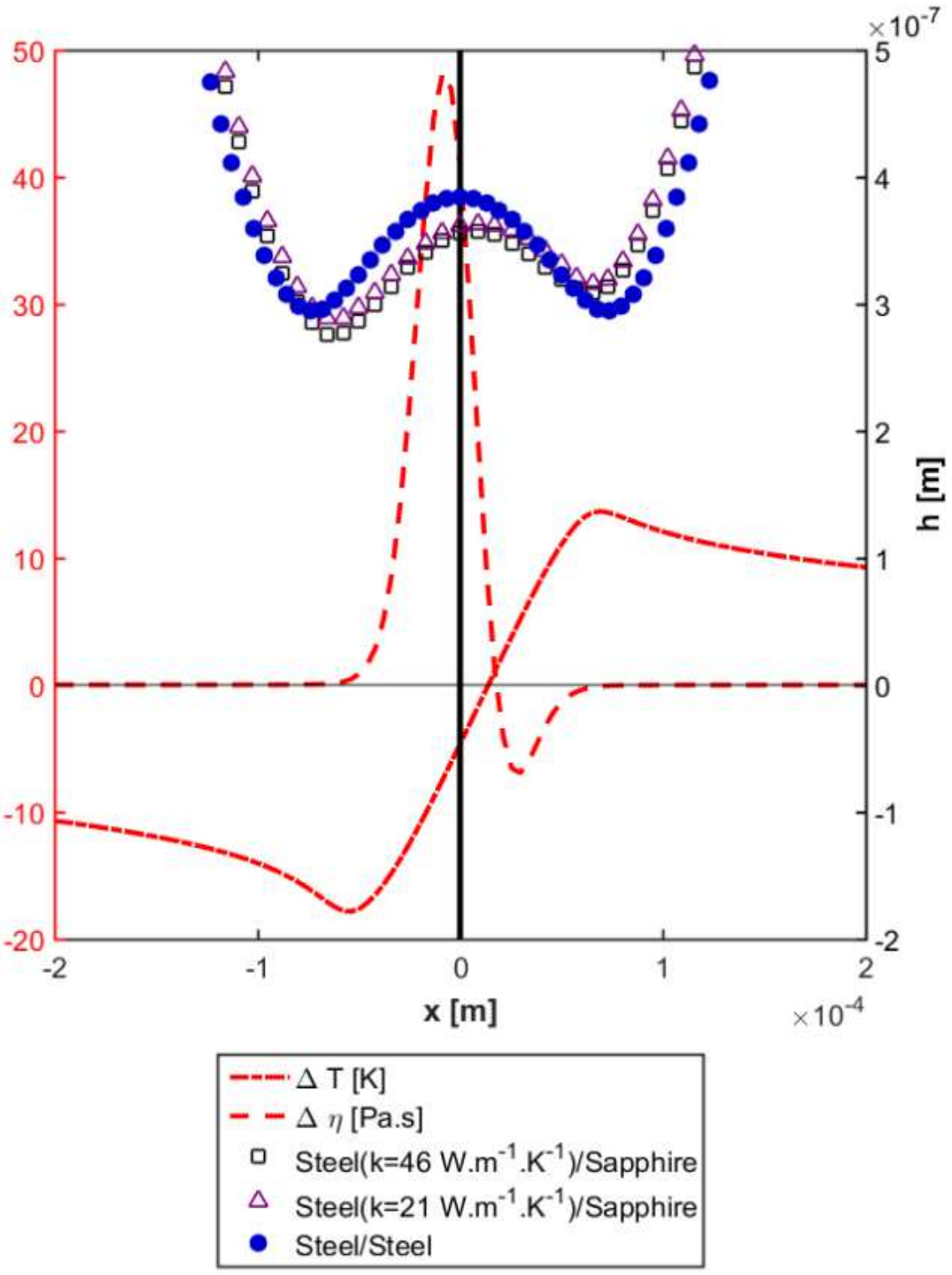

Figure 4 – For the reference case ($u = 5\ m/s$, $w^{1D} = 5.82 \times 10^4\ N.m^{-1}$ and $T_0 = 293.15\ K$): On the left axis, temperature and viscosity differences between the fluid/steel interface and the fluid/sapphire interface for the steel/sapphire contact. On the right axis, numerical film thickness in the steel/sapphire contacts (two different values of k) and the steel/steel contact.

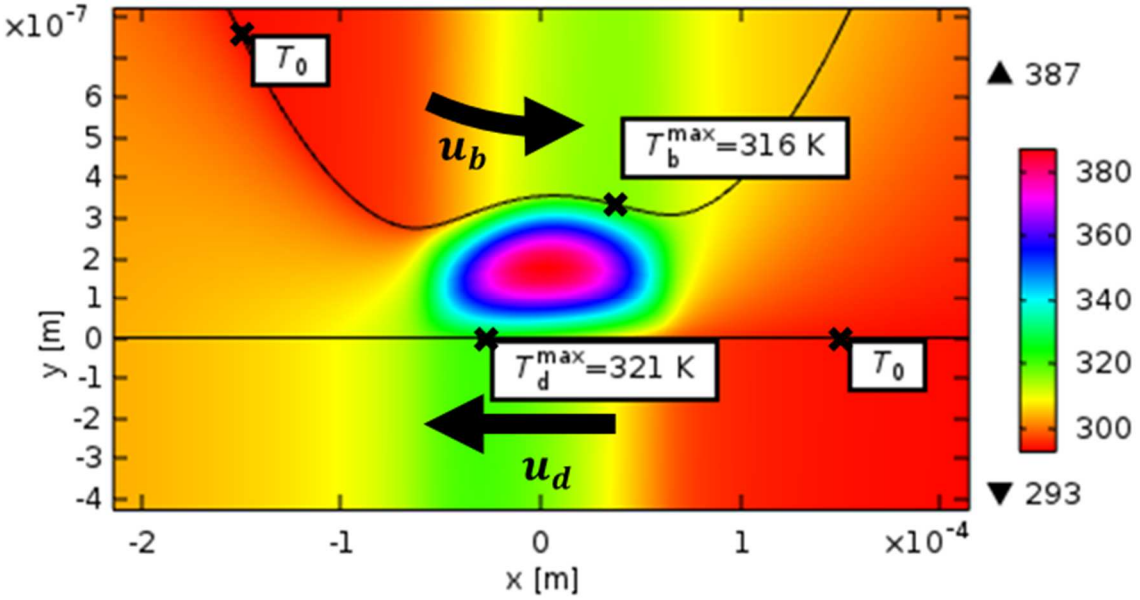

Figure 5 – Temperature variation in the fluid and solids for the reference case ($u = 5\ m/s$, $w^{1D} = 5.82 \times 10^4\ N.m^{-1}$ and $T_0 = 293.15\ K$). The equivalent body displacement is assigned to the top solid (steel). The bottom solid (sapphire) is considered rigid.

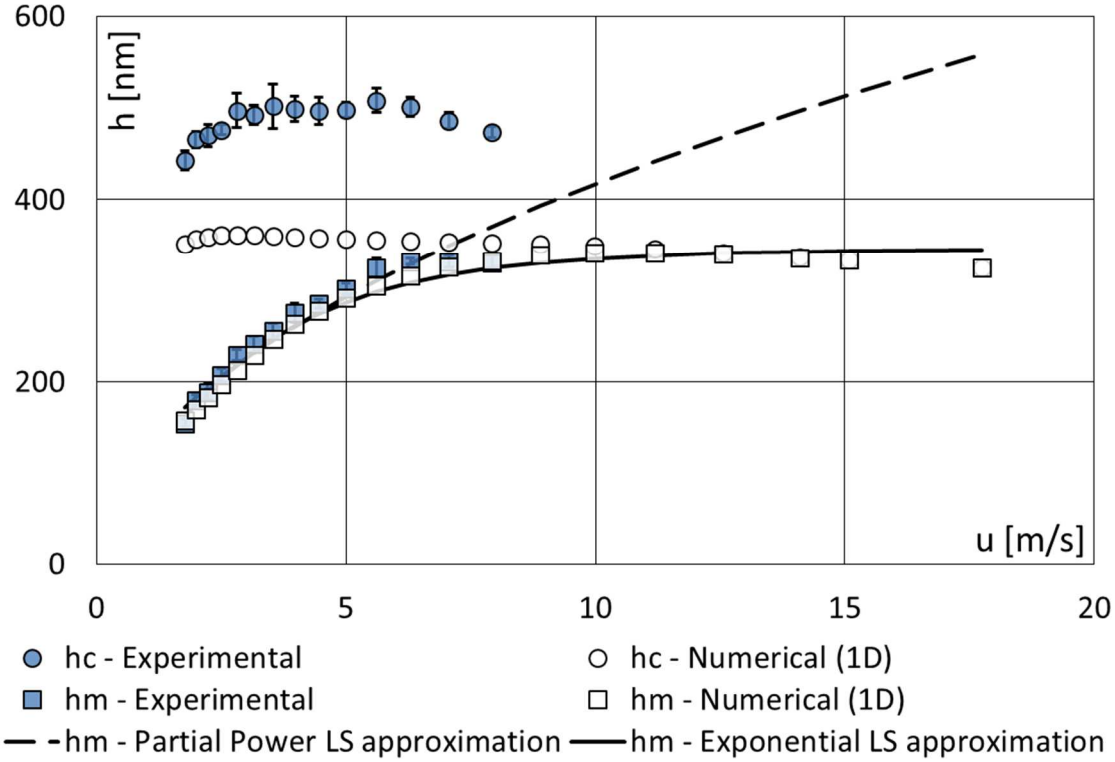

Figure 6 – Central and minimum film thickness variation with the surface velocity at $w^{1D} = 5.82 \times 10^4\ N.m^{-1}$ *and* $T_0 = 293.15\ K$.

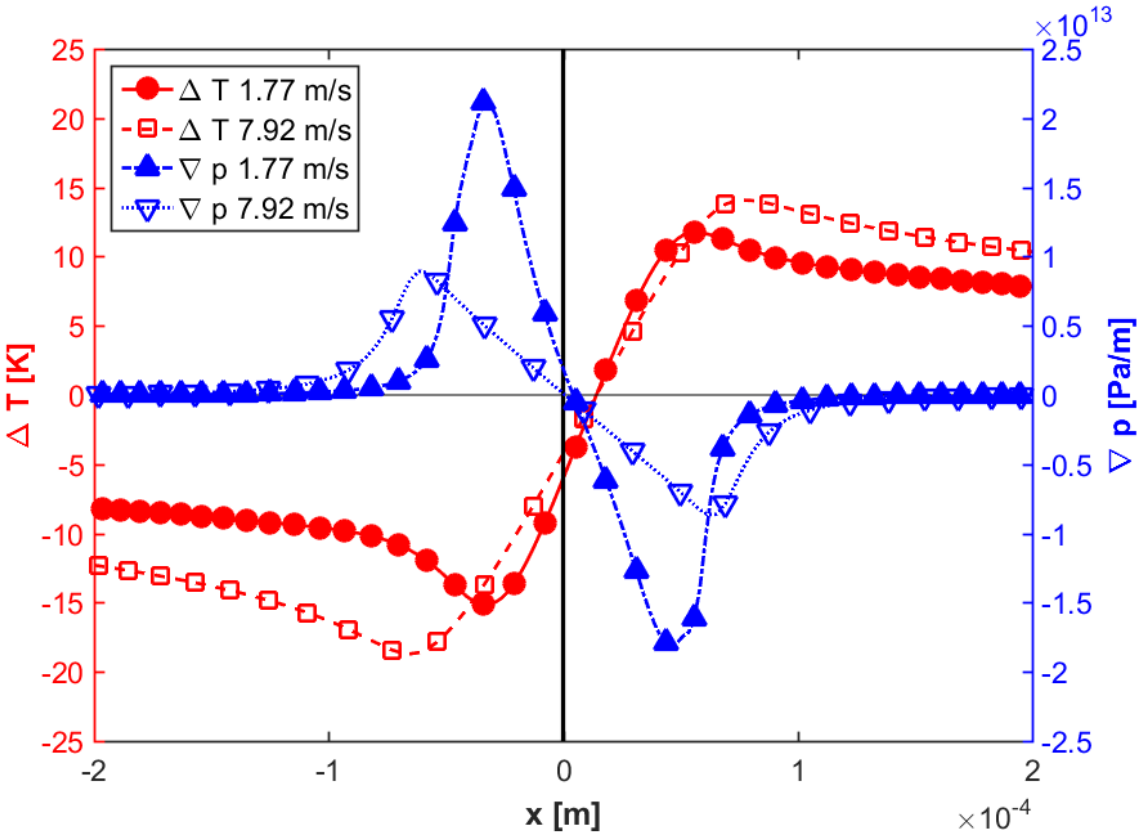

Figure 7 – Temperature differences (in red, left axis) between the two interfaces and pressure gradient (in blue, right axis) in the fluid at $w^{1D} = 5.82 \times 10^4\ N.m^{-1}$ *and* $T_0 = 293.15\ K$*, for two different surface velocities.*

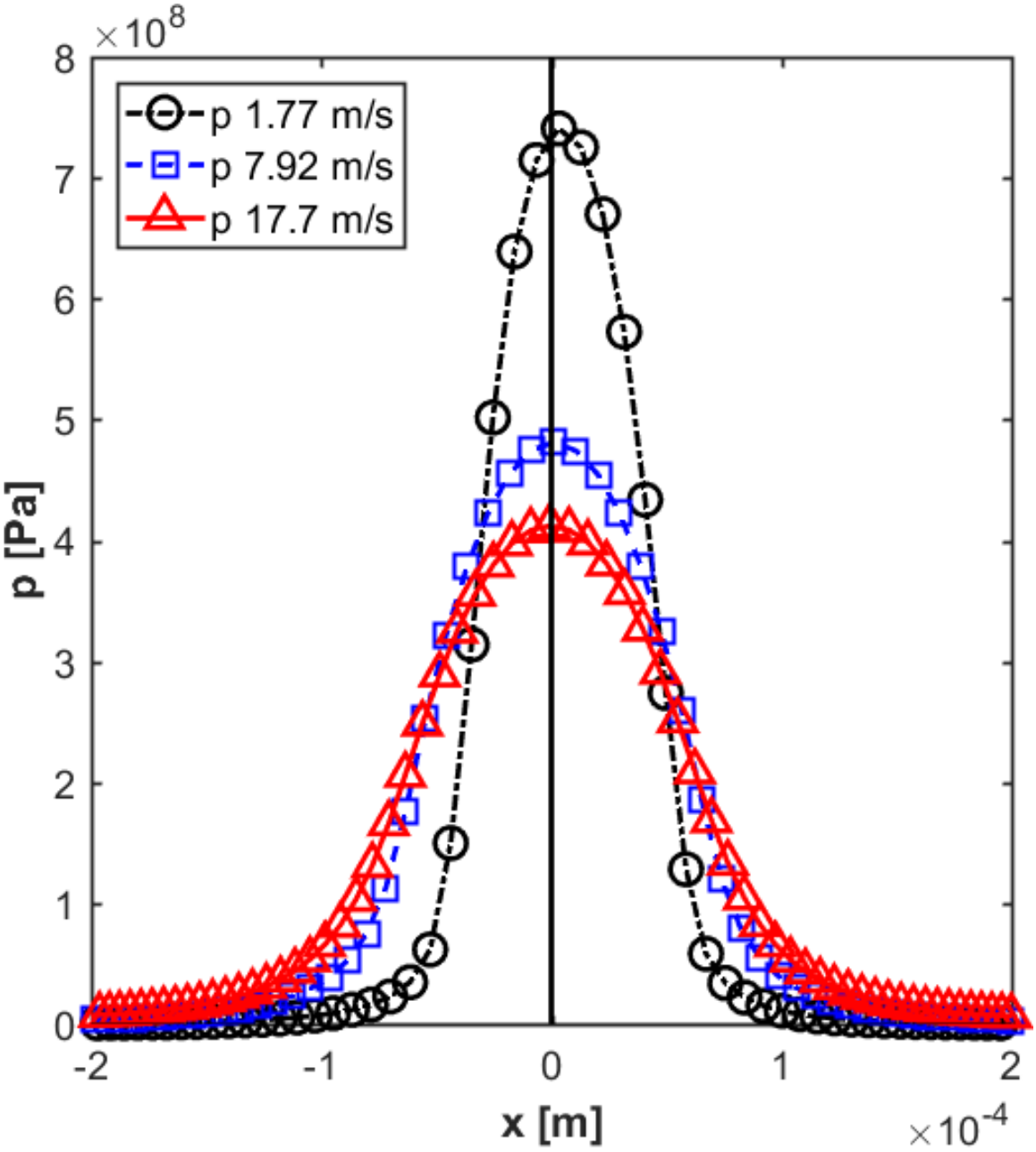

Figure 8 – Pressure profiles at $w^{1D} = 5.82 \times 10^4\ N.m^{-1}$ and $T_0 = 293.15\ K$, for three different surface velocities.

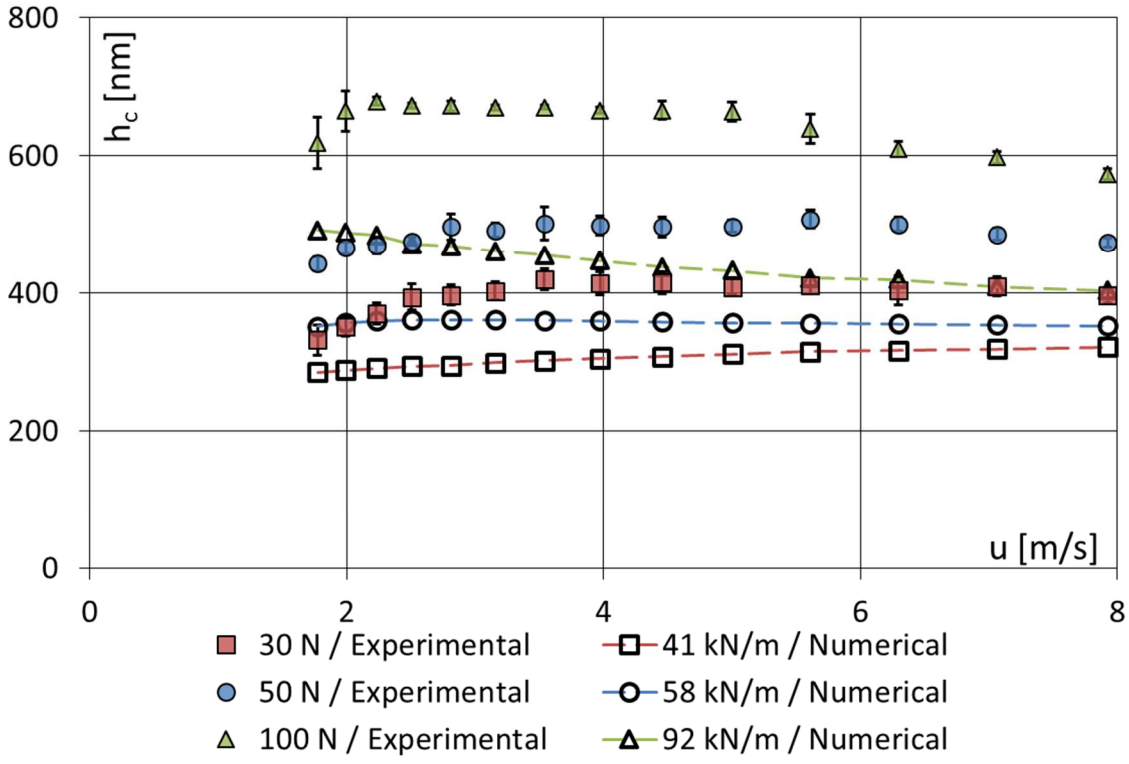

(a)

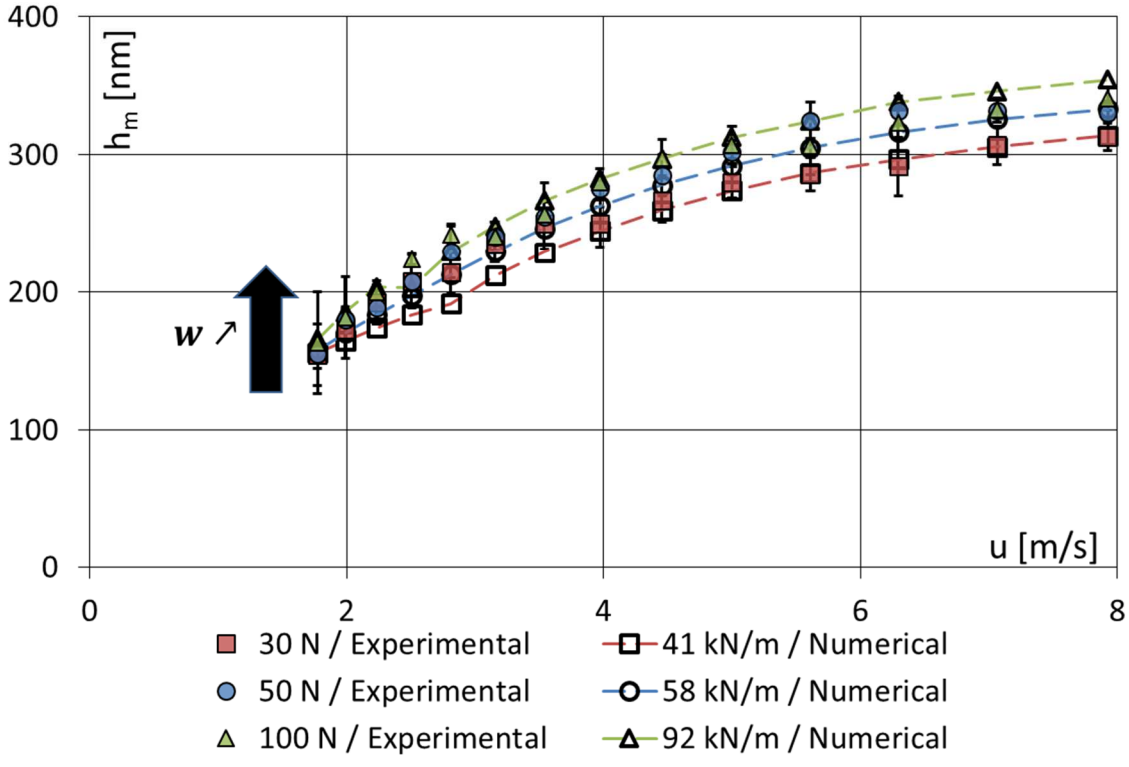

(b)

Figure 9 – (a) Central and (b) Minimum film thickness variation with the surface velocity, for different loads at $T_0 = 293.15\ K$.

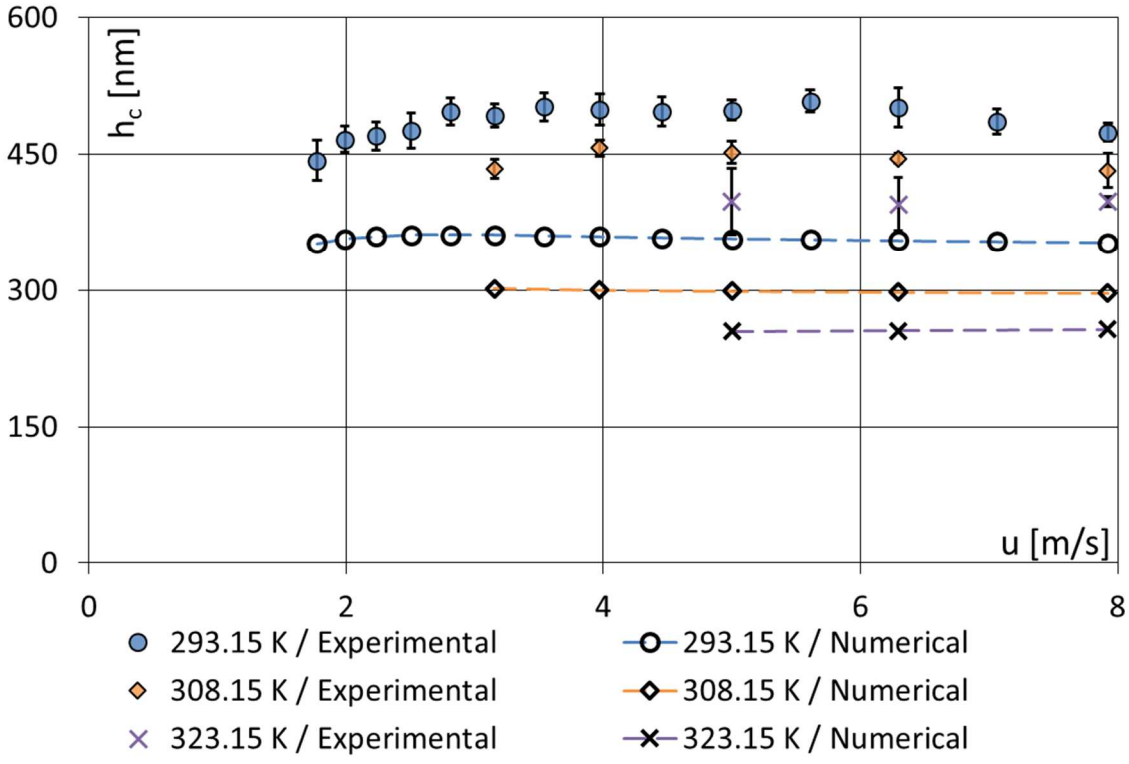

(a)

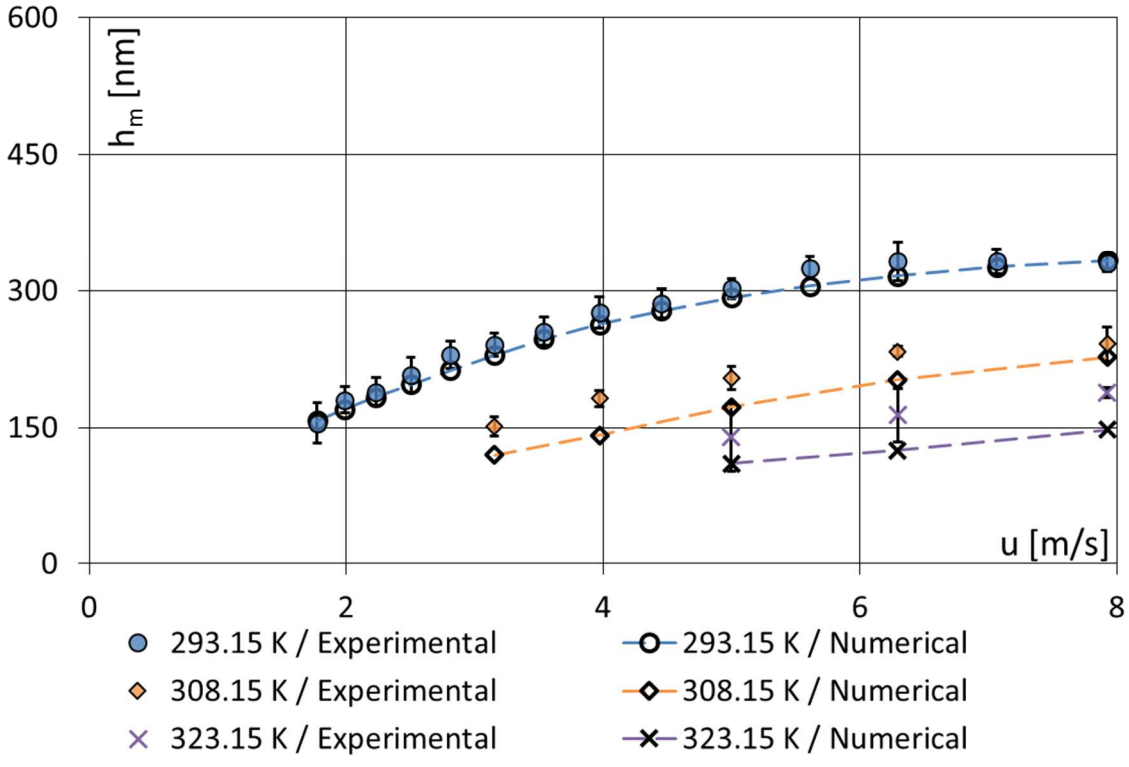

(b)

Figure 10 – (a) Central and (b) Minimum film thickness variation with the surface velocity, for different external temperatures at $w^{1D} = 5.82 \times 10^4\ N.m^{-1}$.

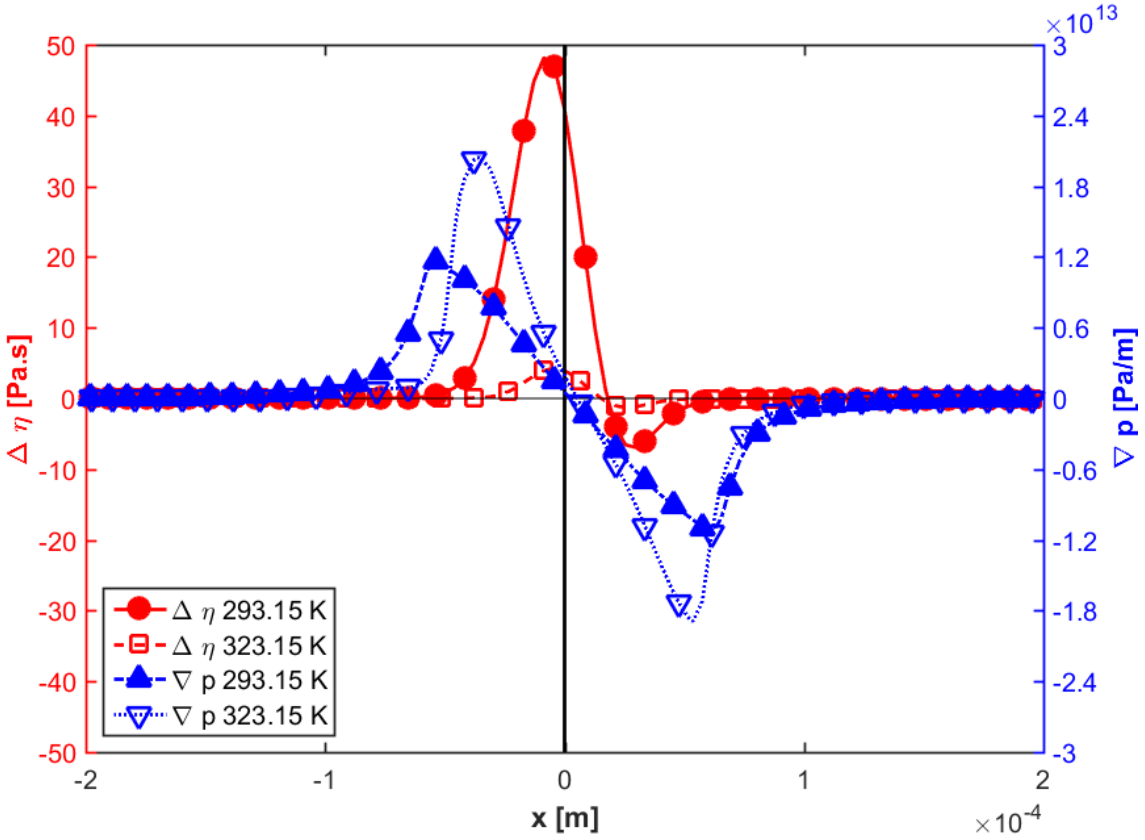

Figure 11 – Viscosity differences (in red, left axis) between the two interfaces and pressure gradient (in blue, right axis) in the fluid at $u = 5\ m/s$ and $w^{1D} = 5.82 \times 10^4\ N.m^{-1}$, for two different external temperatures.

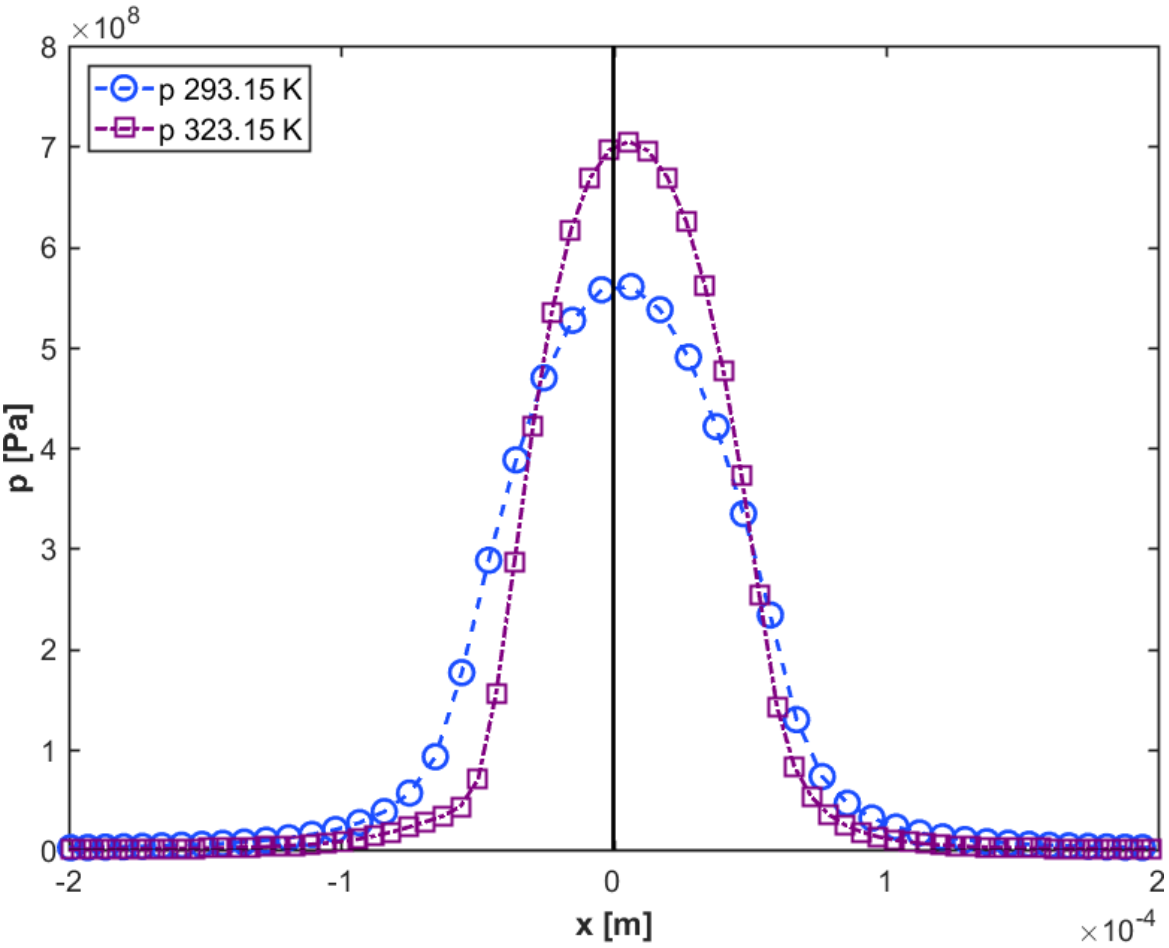

Figure 12 – Pressure profiles at $u = 5\ m/s$ and $w^{1D} = 5.82 \times 10^4\ N.m^{-1}$, for two different external temperatures.

Tables

$T_0\ (K)$	$u(m/s)$	$\mathrm{w}^{2\mathrm{D}}(N)$	$p_h(GPa)$	$\mathrm{w}^{1\mathrm{D}}(N.m^{-1})$	Number of Cases
293.15	$\{1.77; 1.99; 2.26; 2.51; 2.81; 3.16; 3.54; 3.97; 4.46; 5.00; 5.61; 6.30; 7.06; 7.92\}$	30	0.390	4.14×10^4	14
293.15		50	0.462	5.82×10^4	14
293.15		100	0.582	9.24×10^4	14
308.15	$\{3.16; 3.97; 5.00; 6.30; 7.92\}$	50	0.462	5.82×10^4	5
323.15	$\{5.00; 6.30; 7.92\}$	50	0.462	5.82×10^4	3

Table 1 – Sets of measurements

	Steel	Sapphire
$E\ [Pa]$	210×10^9	360×10^9
v	0.3	0.34
$\rho\ [kg.m^{-3}]$	7850	4000
$Cp\ [J.kg^{-1}.K^{-1}]$	470	750
$k\ [W.m^{-1}.K^{-1}]$	46	40

Table 2 – Material properties (from [34]*)*

$Cp_f\ [J.kg^{-1}.K^{-1}]$	1900	$A1$	188.95
$k_f\ [W.m^{-1}.K^{-1}]$	0.118	$A2\ [Pa^{-1}]$	0.533×10^{-9}
$\rho_0\ [kg.m^{-3}]$	872	$B1\ [Pa^{-1}]$	7.37×10^{-9}
$K_{00}\ [Pa]$	9.234×10^9	$B2$	-0.6171
$K_M{}'$	10.545	$Tg_0\ [K]$	204.68
$a_v\ [K^{-1}]$	7.734×10^{-4}	$p_0\ [Pa]$	0
$\beta_k\ [K^{-1}]$	6.09×10^{-3}	a_{CY}	5
$\mu_g\ [Pa.s]$	1×10^{12}	n_{CY}	0.35
$C1$	15.9035	$G_{CY}\ [Pa]$	7×10^6
$C2$	14.1596		

Table 3 – Fluid properties (from [36][37]*)*

Nomenclature

Subscript	Description	
b	Steel barrel	
d	Sapphire disk	
f	Fluid	
0	Reference value	
Superscript	Description	
$1D$	Refers to the line contact model	
$2D$	Refers to the wide point contact model	
Variable	Description	Formula
a_{CY}	Carreau-Yasuda parameter $[-]$	
a_v	Murnaghan parameter $[K^{-1}]$	
A_1	WLF parameter $[K]$	
A_2	WLF parameter $[Pa^{-1}]$	
a^{1D}	Line contact static dimension along $\vec{x}$ $[m]$	$\left(8w^{1D}R_{eq}/\pi E'\right)$^(1/2)
a^{2D}	Wide point contact static dimension along $\vec{x}$ $[m]$	$\left(3w^{2D}R_{b,x}/2E'\right)$^(1/3)
B_1	WLF parameter $[Pa^{-1}]$	
B_2	WLF parameter $[-]$	
b^{2D}	Wide point contact static dimension along $\vec{y}$ $[m]$	$\left(3w^{2D}R_{b,y}/2E'\right)$^(1/3)
C_p	Thermal heat capacity $[J.kg^{-1}.K^{-1}]$	
C_1	WLF parameter $[-]$	
C_2	WLF parameter $[K]$	
D	Ratio of ellipticity $[-]$	$R_{b,x}/R_{b,y}$
E	Young modulus $[Pa]$	
E'	Equivalent Young modulus $[Pa]$	$2/E' = (1-\nu_b^2)/E_b + (1-\nu_t^2)/E_t$
G_{CY}	Carreau-Yasuda parameter $[-]$	
h	Film thickness $[m]$	
h_c	Central film thickness $[m]$	
h_m	Average minimum film thickness $[m]$	$(h_m^- + h_m^+)/2$
h_m^-	Lowest local minimum film thickness $[m]$	
h_m^+	Highest local minimum film thickness $[m]$	
h_0	Rigid body separation $[m]$	
k	Thermal conductivity $[W.m^{-1}.K^{-1}]$	
K_{00}	Murnaghan parameter $[Pa]$	
K_0'	Murnaghan parameter $[-]$	
n_{CY}	Carreau-Yasuda parameter $[-]$	

p	Pressure $[Pa]$	
p_0	Room pressure $[Pa]$	
p_h^{1D}	Line contact Hertz pressure $[Pa]$	$2w^{1D}/\pi a^{1D}$
p_h^{2D}	Wide point contact Hertz pressure $[Pa]$	$3w^{2D}/2\pi(a^{2D})^2$
R_{eq}	Equivalent line contact radius $[m]$	
$R_{b,x}$	Primary radius of the barrel $[m]$	
$R_{b,y}$	Secondary radius of the barrel $[m]$	
S_a	Average surface roughness $[nm]$	
T_0	External temperature $[K]$	
T_{g0}	Glass transition temperature of the fluid $[K]$	
u	Surface velocity $[m/s]$	
$\vec{U}$	Velocity vector	
w^{1D}	Linear Load $[N.m^{-1}]$	
w^{2D}	Load $[N]$	
∇p	Pressure gradient along $\vec{x}$ $[Pa/m]$	$\nabla p = \partial p/\partial x$
$\dot{\gamma}$	Shear rate $[s^{-1}]$	
δ	Equivalent displacement $[m]$ – Always negative	
Δ	Difference between top and bottom interfaces	
η	Non-Newtonian viscosity $[Pa.s]$	
μ	Newtonian viscosity $[Pa.s]$	
μ_0	Newtonian viscosity at T_0 $[Pa.s]$	
μ_g	Viscosity at T_{g0} $[Pa.s]$	
ν	Poisson ratio $[-]$	
ρ	Density $[kg.m^{-3}]$	
ρ_0	Density at $T_0 = 20°C$ $[kg.m^{-3}]$	
τ_e	Normal value of the shear stress $[Pa]$	
τ_{zx}	Shear stress along $\vec{x}$ $[Pa]$	
τ_{yx}	Shear stress along $\vec{y}$ $[Pa]$	